Weather and Climate Extremes 38 (2022) 100529

Contents lists available at ScienceDirect

Weather and Climate Extremes

journal homepage: www.elsevier.com/locate/wace

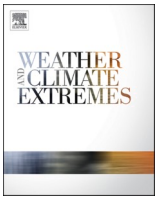

Attribution of the human influence on heavy rainfall associated with flooding events during the 2012, 2016, and 2018 March-April-May seasons in Kenya

Joyce Kimutai [a,b,*], Mark New [a], Piotr Wolski [c], Friederike Otto [d]

[a] African Climate Development Institute, University of Cape Town, Cape Town, South Africa
[b] Kenya Meteorological Department, Nairobi, Kenya
[c] Climate Systems Analysis Group, University of Cape Town, South Africa
[d] Grantham Institute, Imperial College, London, UK

ARTICLE INFO

Keywords:
Extreme rainfall
Extreme event attribution
Factual and counterfactual
Magnitude ratio
Attributable magnitude

ABSTRACT

The changing probabilities of extreme climate and weather events, in terms of frequency, intensity, spatial extent, duration, and timing is one of the most noticeable and damaging manifestations of human-induced climate change. During the March-April-May (MAM) rainfall season of 2012, 2016 and 2018, Kenya experienced high rainfall that caused both widespread and localised flooding, resulting in human and livestock deaths, destruction of infrastructure and property, bursting of riverbanks, submerging of farmlands and emergence of isolated cases of water-borne diseases. Here, we aim to quantify how the magnitude of heavy rainfall during these seasons may have been altered by human-induced climate change. We undertake a probabilistic attribution analysis using three different approaches utilising two observational datasets and two independent climate model experiment set-ups. We analyse three different seasonal heavy rainfall indices, maximum consecutive 5-day, 10-day, and 20-day rainfall, to compare the magnitude of maxima recorded in MAM 2012, 2016 and 2018 with the magnitude of maxima in a pre-industrial climate (with little or no anthropogenic influence). We find a shift towards intensification of extreme rainfall in today's climate, although these increases are not in all cases statistically distinguishable from our estimates of magnitudes in the preindustrial climate. Although we find no significant anthropogenic climate change influence, the intensification of extreme rainfall amid the observed drying trend and the projected increases in rainfall in the MAM season in Kenya, leave the already vulnerable societies with uncertainties about how to prepare for a changing climate. This study, therefore, provides a basis for an in-depth assessment of current and future trends of extreme rainfall in East Africa in adapting to changing climate risks for sustainable development in the already vulnerable and less resilient society.

1. Introduction

The Greater Horn of Africa has experienced a number of extreme weather and seasonal climate events over the past two decades (Liebmann et al., 2014; Philippon et al., 2015; Hoell et al., 2017; Uhe et al., 2018; Funk et al., 2018; Kilavi et al., 2018). While droughts have predominated, several heavy precipitation events with devastating impacts on agricultural systems, infrastructure, settlements, property, and life have also been recorded. During the March-April-May (MAM) "long rains" seasons of 2012, 2016, and 2018, several parts of Kenya experienced extremely high rainfall causing widespread flooding and landslides (Fig. 1). In MAM 2018 all meteorological stations in the country recorded rainfall exceeding the long-term mean, and at many stations, that season has turned out to be the wettest MAM on operational record so far. By 7 May 2018, at least 311,164 people had been displaced by floods across the country, at least 132 had died, and a further 33 were injured (OCHA, 2018; Kenya Govt, 2018). Additionally, 47 deaths were reported after Solai Dam in Nakuru County could not withstand the floods and burst on 9 May. Very heavy rainfall was also recorded over several periods during the MAM seasons in 2016 and 2012 across the country, but the severity was not as high as in 2018. Many stations recorded seasonal rainfall above their long-term means, especially in the central and western parts of the country. In 2012, at least 8,450 acres of farmland were submerged following bank bursting along the Tana,

* Corresponding author. African Climate Development Institute, University of Cape Town, Cape Town, South Africa.
E-mail address: kimutaijoy@gmail.com (J. Kimutai).

https://doi.org/10.1016/j.wace.2022.100529
Received 5 January 2022; Received in revised form 13 November 2022; Accepted 15 November 2022
Available online 23 November 2022

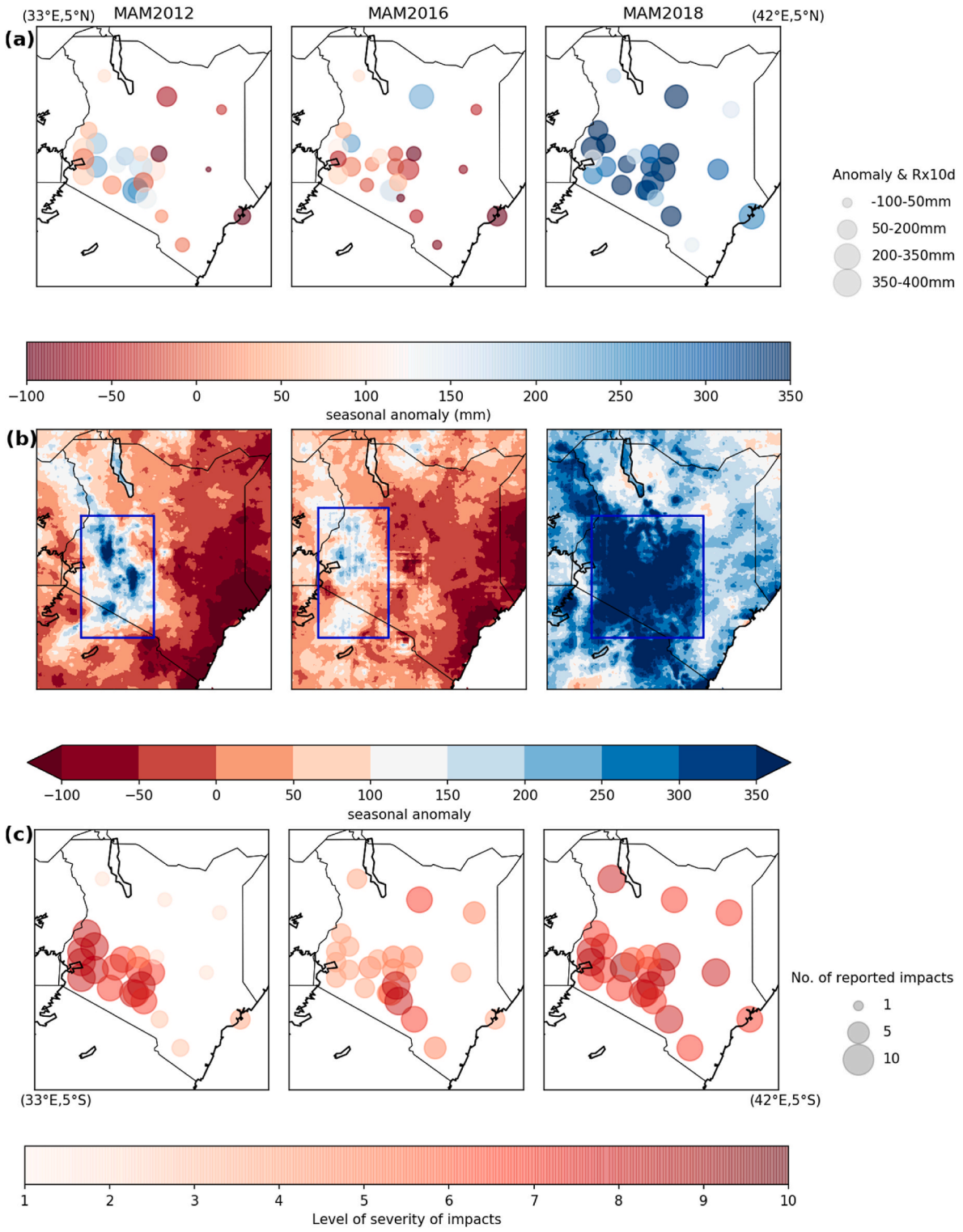

Fig. 1. Spatial distribution of season total rainfall anomalies during the MAM 2018, 2016, and 2012 seasons and the recorded impacts of associated flood events in Kenya. Anomalies in seasonal mean rainfall based on Kenya Meteorological Department (KMD) station data (a), CHIRPS gridded dataset (b) (see description, section2.1) in reference to the 1981–2016 climatological period and their associated impacts (c). In (a), the size of the circle corresponds to the maximum 10-day consecutive rainfall (Rx10d) amount, while the colour shows the seasonal anomaly. For (c), the circle size corresponds to the number of reported cases of flood impacts while the colour saturation shows the level of severity. Due to an unavailability of monetary values of impact losses, the impacts are rated on a scale of 1–10 based on the following criteria: we consider reported deaths, landslides, river/dam bursts and displacement of people as the most severe with a rating of 7–10; isolated cases of water-borne diseases and submerged farmlands as of moderate severity with a rating of 4–6; and impassable roads as of minimal severity with a rating of 1–3. Boxes in (b) show the region(s) of study for each year. (For interpretation of the references to colour in this figure legend, the reader is referred to the Web version of this article.)

Ewaso Nyiro, Yala, and Nyando rivers, and some bridges were swept away, rendering roads impassable (OCHA, 2012). In 2016, an estimated total of 34,129 people were affected by the floods, with informal settlements in the Nairobi metropolitan area being the worst impacted, including the collapse of a residential building on 29 April 2016 that caused 16 fatalities (IFRC, 2016).

A number of previous studies have investigated whether and to what extent human-induced climate change played a role in recent weather and climate extremes in East Africa, but these focused on drought and the observed long-term drying trend of the long rains (Funk et al., 2013, 2018; Lott et al., 2013; Funk and Hoell, 2015; Liebmann et al., 2014; Marthews et al., 2015; Uhe et al., 2018).The answer to these attribution questions depends strongly on the framing (Otto et al., 2016). Hoell et al. (2017) and Funk et al. (2018) linked the increasing frequency of drier MAM seasons in the period 1981–2016 to warming Indo-Pacific Sea surface temperatures (SSTs), with strong anthropogenic influence on the north-western Pacific associated with intensification of Indian Ocean branch of the Walker Circulation. Similarly, Liebmann et al. (2014) linked the observed MAM 1979–2012 drying trend to the sensitivity of weather systems to increased zonal SST gradient between Indonesia and the central Pacific, which was attributable to climate change. Lott et al. (2013) concluded that human influence on climate enhanced the probability of rainfall anomalies at least as dry as that of the MAM 2011 drought in East Africa by a small factor. On the other hand, Lyon 2014, linked the post-1998 decline in MAM rainfall to natural multidecadal variability in the tropical Pacific rather than human-induced climate change. Marthews et al. (2015) and Uhe et al. (2018) found no anthropogenic influence on the likelihood of low rainfall observed during the 2014 MAM and 2016 October-November-December (OND) 'short rains' respectively, although they could not rule out the influence on other variables like surface air temperature and net incoming radiation at the surface. Kew et al. (2021) repeated several of the previous studies with multiple models, and investigated the role of soil moisture and evaporation, concluding there was an absence of a statistically significant human-influenced climate signal in the periods of lower rainfall. They pointed out that finding whether climate change exacerbated the droughts depends on which methods are used to calculate water demand as a function of moisture availability and evaporative demand.

The influence of climate change on the severity of recent extreme flood events amid the general drying trend remains even more uncertain. Several studies have looked at the dynamics associated with interannual and intraseasonal variability of the long rains (Camberlin and Okoola, 2003; Pohl and Camberlin, 2006a; Hastenrath et al., 2010; Omondi et al., 2012; Hogan et al., 2015; Vellinga and Milton, 2018) but only a handful have investigated the possible influence of climate change on the processes, dynamics, and drivers. So far, there have not been any heavy rainfall attribution studies in the region. The main drivers of MAM rainfall variability are related to zonal wind anomalies, zonal propagation of convection, advection of moisture and SST anomalies in the Indian and the Pacific Oceans (Pohl and Camberlin, 2011; Vigaud et al., 2016; Nicholson, 2017). The 'East African climate paradox' (Rowell et al., 2015) where an increased frequency of droughts and a general drying trend has been observed since the early 1990s (e.g., Funk et al., 2008; Nicholson, 2016a) while global climate model projections show increases in rainfall (Meehl et al., 2007; Otieno and Anyah, 2012) has spawned scientific interest. Few hypotheses have been presented to explain this paradox. Giannini et al. (2018), argued that confidence and reliance in projections of future increase in rainfall in East Africa is limited due to substantial biases in simulations of the regional climate, and discrepancy in the modelled versus observed tropical Pacific and Indian SST trends. They pointed out the role and effect of the complex East African topography in the advection of moisture from the Indian Ocean and Congo Basin, and whether the current cooling of the tropical eastern Pacific is due to internal variability alone or partly attributable to evolving La Niña-like conditions due to increasing GHGs in the atmosphere. Tierney et al. (2015) demonstrated how simulated El-Niño-like shifts tend to unrealistically increase annual rainfall through the effects of overestimated short rains since most models misrepresent the annual and seasonal cycle by overestimating the short rains and underestimating the long rains.

In principle, every extreme event is unique and usually results from a combination of external drivers, natural and anthropogenic, as well as climate system internal (random or unresolved) variability (Stott et al., 2016). The presence of an external driver like human-induced climate change can alter the likelihood of occurrence of an extreme weather or climate event. This study aims to investigate the contribution of anthropogenic forcing of climate on the magnitude of the flood-producing rainfall during the 2012, 2016, and 2018 MAM seasons in Kenya. Focusing on three different MAM seasons allows for investigation of a wider set of cases in the possible responses to anthropogenic forcing and natural variability, thus enhancing confidence in the attribution results. The focus is on the sub-seasonal characteristics of heavy rainfall associated with the surface flooding rather than the overall trend in the MAM rains. The scientific question we pose is: has the magnitude of 2012, 2016, and 2018 MAM heavy rainfall that occurred at the time of widespread flooding in Kenya been altered by anthropogenic climate change? We focus on three heavy rainfall indices, the 5-day, 10-day and 20-day seasonal maxima, which capture a range of possible flood-inducing rainfall processes, from shorter intense events to longer more persistent rainfall that leads to flooding through saturation of the soil. This paper is structured as follows: section 2 describes the observational data and model simulations used in the study, and the analysis methods including model evaluation and the attribution approach(es); the results of model evaluation and attribution analysis are provided in Section 3, together with synthesised results; a discussion and conclusions are given in section 4.

2. Data and methods

Flood events can arise from different forms of rainfall extremes; short intense events or longer events resulting from multi-day accumulations. To classify the three MAM events, we define the heavy rainfall in a way that best represents what caused the impacts and reflects the extremity of the meteorological event, to guide the statistical analysis of the observations and model experiments (NAS, 2016; Otto, 2017). In the case of flood events considered here, there is no clear definition of what aspects of the observed rainfall events (e.g., duration and intensity) caused any single flood. Therefore, we chose to assess three different heavy rainfall indices: maximum consecutive 5-day, 10-day, and 20-day precipitation (Rx5d, Rx10d, and Rx20d) (Zhang et al., 2011; Sillmann et al., 2013). We then employ the multi-method multi-model event-attribution approach (Hegerl and Zwiers, 2011; Otto et al., 2016; NAS, 2016; Hannart et al., 2016) applied routinely to attribution studies (e.g., Van Oldenborgh et al., 2016; Haustein et al., 2016; Uhe et al., 2018; Sun and Miao, 2018; Herring et al., 2018; Philip et al., 2019) to estimate changes in magnitudes of these indices that are attributable to human-induced climate change. We use two different observational data sets and multiple climate model simulations of varied experimental setups, in each case independently applying an experiment-specific attribution methodology. This multi-method and multi-model approach is geared towards enhancing confidence in the findings and in the final overall attribution statement(s) (Philip et al., 2020).

2.1. Observational data

Observational data are the basis for determining the magnitude-likelihood characteristics, as well as the spatial extent, of the analysed events. The results are strongly conditional on data quality and particularly on the duration of the available time series. Here, we used two observational daily rainfall datasets: (i) Kenya Meteorological Department (KMD) meteorological station data; and (ii) the Climate Infrared

Precipitation with Stations (CHIRPS) satellite-based gridded data. For KMD data, we used daily rainfall records from 17 synoptic weather stations within the study area(s) for the period 1981–2018 (see Supplementary Material S1 for station details and Fig. 1 for locations). We obtained an area average of the station data over the analysis domain (see below) using the Thiessen polygon approach (Thiessen, 1911) since our interest is on a regionally constrained exceedance of flood-relevant amounts of rainfall, at scales suitable for analysis by climate models. CHIRPS is a high-resolution (0.05°) daily precipitation dataset, available from 1981-present. CHIRPS uses the Tropical Rainfall Measuring Mission Multi-Satellite Precipitation Analysis version 7 (TMPA 3B42 v7) to calibrate global Cold Cloud Duration (CCD) rainfall estimates (Funk et al., 2015). It includes monthly precipitation climatology, and atmospheric model rainfall fields from the NOAA Climate Forecast System, version 2 (CFSv2). It is blended with station data to produce a gridded rainfall time series suitable for trend analysis, and seasonal flood and drought monitoring. We used daily data for the period 1981–2018.

2.2. Climate models and experiments

2.2.1. Atmospheric General Circulation Models (AGCMs)

Atmospheric General Circulation Models (AGCMs) are primarily designed to isolate the component of atmospheric variability driven by oceanic boundary forcing. AGCMs are less computationally demanding hence more simulations at higher spatial resolution can be obtained aimed at improving signal-to-noise ratio. We employ ensemble simulations from three attribution-dedicated experiments: ECHAM5.4, CAM5.1, and weather@home2. ECHAM5.4 and CAM5.1 participated in the Climate of the 20th Century Plus (C20C+) Detection and Attribution project (Stone et al., 2019) while weather@home2 (Guillod et al., 2017) simulations were produced by the www.climateprediction.netdistributed system based at the University of Oxford. For each model, we utilise two sets of simulations: historical and natural, which serve as factual and counterfactual worlds for the attribution analysis. Historical runs are simulations representing possible states of the atmosphere and land surface for all years of 20th and 21st century under observed SST, land surface and sea ice boundary conditions, along with historical radiative forcing. Here, we analyse outputs for MAM 2012, 2016, and 2018. Natural simulations represent possible states of the atmosphere under an estimate of what the observed boundary conditions might have been in the absence of anthropogenic interference with the climate system. Detailed experiment descriptions are laid out in Table 1 and further documentation and outputs from the CAM5.1 and ECHAM5.4 and simulations can be found online: (https://portal.nersc.gov/c20c/data), (https://www.esrl.noaa.gov/psd/repository/alias/facts) and respectively. weather@home data is archived at (https://jasmin.ac.uk/). The data will be made available through OpenUCT which is an open-access data portal.

2.2.2. General circulation models (CGCMs)

Comprehensive coupled climate models allow a dynamically interacting ocean; therefore, assumptions on the influence of anthropogenic climate change on ocean variability and on the effects of short-term coupled atmosphere-ocean interactions on the production of extreme weather and climate events are minimised. However, the simulated SSTs do not track those observed, so daily to decadal internal variability, and the timing of specific events, are not captured in these experiments. We employed 7 models from the sixth phase of Coupled Model Intercomparison Project (CMIP6; Eyring et al., 2016), which were selected after evaluation from the 15 (Table 2) for which daily rainfall data were available (see section 3). For models with more than one simulation, only the first member of the ensemble was utilised as the use of many members would skew the results since some models have more members than others. Thus, the choice of the first member is arbitrary as ensemble members only differ by initial conditions. We use historical simulations covering the period 1850–2014, and then extend the data to 2030 using simulations driven by the SSP1-2.6 (shared socio-economic pathway) scenario, which is closest to the current forcing for our averaging period, as the forcing does not increase as steeply into the future. For attribution, we consider two climate worlds: historical and natural. We take 1850–1900 to represent the natural climate, representative of the period prior to the onset of large-scale industrialization and human influence on the climate. This approach has been used in several studies (e.g., Van Oldenborgh et al., 2016; Uhe et al., 2017) to understand the pre-industrial climate. While cognizant of other approaches such as the use of historicaNat runs, not all the coupled models used in this analysis have such data available. For the historical climate, we consider the period 2000–2030 centred on 2015. For all the SSP scenarios, climate conditions in the next 15–20 years are not projected to be significantly different from each other nor depart significantly from the current climate conditions. Therefore, we assume the average forcing over this 30-year period is roughly equal to the forcing during the period 2012–2018. And for consistency with the historical simulations, the use of the first member is maintained. Further documentation and outputs from the CMIP6 experiments can be found online (https://esgf-node.llnl.gov/projects/cmip6/).

2.3. Model evaluation

Precipitation extremes in Eastern Africa are influenced by a complex interaction of changes in local weather systems and perturbations in the global and regional circulation (Nicholson 2017; Vellinga and Milton,

Table 1
A description of Atmosphere-only model experiments.

Model	Experiment	Description	Citation
CAM5.1	All-Hist/est1 300 simulations	2012, 2016, and 2018 observationally derived SSTs and sea ice, GHG concentrations, sulphate aerosol burden, organic aerosol burden, black carbon aerosol burden, dust aerosol burden, sea salt aerosol burden, ozone concentrations, solar insolation, volcanic aerosol, land surface cover/use. Prescribed model aerosol values are used for the non-volcanic aerosols; volcanic aerosols are prescribed through a height-latitude profile of the mass mixing ratio.	Neale et al., (2012);
	Nat-Hist/CMIP5-est1 300 simulations	1855 GHG concentrations, aerosol burdens, SST and Sea Ice extent, and ozone concentrations. Solar and volcanic forcing is identical to All-Hist/est1.	Stone et al. (2018)
ECHAM 5.4	AMIP, Observed Radiative Forcing 50 simulations	2012, 2016 & 2018 AMIP conditions with specified historical time varying GHG and ozone. The GHG evolution is based on observed estimates from 1979 to 2005, and then an RCP6 scenario thereafter. The time-varying ozone is based on data from the AC&C/SPARC ozone database.	Roeckner et al., (2003);
	AMIP with 1880s Radiative Forcing 50 simulations	AMIP conditions in which the SST has been detrended and adjusted to 1880 equivalent mean conditions (the SST otherwise retain identical interannual and decadal variability as in the other experiments). Sea ice is set to a repeating seasonal cycle of roughly 1979–1990 (pre-emergence of the melt out). The GHG and ozone concentrations are adjusted to their 1880 values.	Roeckner et al. (2006)
weather @home2	Historical 798 simulations for 2012, 615 for 2016, and 908 for 2018	2012, 2016, and 2018 SSTs and sea ice as observed, other forcings as RCP4.5.	Guillod et al. (2017)
	Natural 1 131 simulations for 2012, 933 for 2016, and 1 610 for 2018	2012, 2016, and 2018 SSTs reconstructed for pre-industrial conditions, all other forcing set to pre-industrial. The maximum observed sea-ice extent is used.	

Table 2
List of CMIP6 models evaluated. Those utilised are asterisked (Expansions of acronyms are available online at https://www.ametsoc.org/ams/list-of-acronyms-and-abbreviations/).

Model	Resolution	Institution	Citation
CNRM-CM6-1-HR*	0.5° in the atmosphere, 0.25° in the ocean, 12 vertical levels	Centre National de Recherches Météorologiques, France	Voldoire et al. (2019)
IPSL-CM6A-LR*	2.0° × 2.0°, 39 layers in the vertical in both the atmosphere and ocean	Institute Pierre-Simon Laplace Climate Modelling Centre, France	Boucher et al., (2020); Lurton et al., (2020)
INM-CM5*	2 × 1.5°, 73 vertical levels in the atmosphere; 0.5 × 0.25°, 40 levels in the ocean	Institute for Numerical Mathematics, Russian Academy of Science, Russia	Volodin and Gritsun, (2018); Volodin et al., (2017)
NorESM2-MM*	1° × 1° in both atmosphere and ocean, 32 vertical layers	NorESM Climate modelling Consortium, Norway	Seland et al. (2020)
UKESM1-0-LL*	1.25° × 1.875°, 85 vertical levels in the atmosphere and 1°, 75 vertical levels in the ocean	Met Office Hadley Centre, UK	Sellar et al. (2019)
NESM3*	1.9°, 47 vertical levels in the atmosphere; 1°, 46 vertical levels in the ocean	Nanjing University of Information Science and Technology, China	Cao et al. (2018)
MRI-ESM2-0*	1° × 1° in both atmosphere and ocean, 80 vertical layers	Meteorological Research Institute (MRI) of the Japan Meteorological Agency	Yukimoto et al. (2019)
CanESM5	2.8° in the atmosphere, 1° in the ocean, 49 vertical layers	Canadian Centre for Climate Modelling and Analysis	Swart et al. (2019)
CESM2-FV2	1.25° × 0.96°, 32 vertical levels in the atmosphere and 1.25° × 0.27°,60 vertical levels in the ocean	National Centre for Atmospheric research, Climate and Dynamics Laboratory	Danabasoglu et al. (2020)
EC-EARTH3	1° in both atmosphere and ocean, 91 vertical levels in the atmosphere, 75 levels in the ocean	European Research Consortium (EC-EARTH)	Döscher et al. (2021)
MIROC6	2.5° in the atmosphere, 81 levels and 2.5°, 63 levels in the ocean	JAMSTEC, Japan	Tatebe et al. (2019)
SAMO-UNICON	1.25° × 0.94 in both atmosphere and ocean, 30 vertical levels in the atmosphere, 60 levels in the ocean	Seoul National University, South Korea	Park & Shin, 2019
TaiESM1	0.9 × 1.25°, 30 vertical levels in the atmosphere and 1°, 60 levels in the ocean	Research Centre for Environmental Changes, Taiwan	Lee et al. (2020)
HadGEM3-GC31-MM	1°,85 vertical levels in the atmosphere and 0.25°, 75 levels in the ocean	Met Office Hadley Centre, UK	Andrews et al. (2020) Gutjahr et al. (2019)
MPI-ESM1-2-HR	T255,95 vertical levels in the atmosphere and 0.4°, 40 levels in the ocean	Max Planck Institute for Meteorology	

2018; Ongoma et al., 2018a,b). There is limited understanding of the influence of regionally important forcings such as aerosols and land-use changes on weather and climate (Rowell et al., 2016), remote forcing control and inadequate simulation of the regional climate by many climate models (Giannini et al., 2018). These important factors pose a challenge in application of models to understanding changes in extremes over the region (Otto et al., 2015, 2020; Nicholson 2017; Otto et al., 2020a,b). We, therefore, pay particular attention to a reliable representation of observed rainfall by models for their application in this study. We focus on model ability to realistically simulate MAM spatio-temporal patterns of seasonal and heavy rainfall over the study region. In this assessment, we use three main error-based metrics; Mean Absolute Error (MAE), Pearson correlation coefficient (R) and Root Mean Squared Error (RMSE) on different rainfall characteristics: (i) seasonal cycle (hereafter, SC) patterns to assess models' ability to replicate the expected bimodal rainfall regime (AGCMs & CGCMs); (ii) spatial patterns of mean MAM rainfall (AGCMs & CGCMs); and (iii) the temporal (interannual) variability of MAM rainfall (AGCMs only). We also make use of quantile-quantile (Q-Q) plots to evaluate the modelled versus observed distributions of Rx5d, Rx10d, and Rx20d (for convenience hereafter, RxNds). We calculate the agreement statistics for the models against observations (CHIRPS) and also ERA5 against CHIRPS, after which we compare the performance of the models against that of ERA5. ERA5 (ECMWF Reanalysis 5th Generation) data is incorporated in the evaluation to serve as a benchmark for the models — data assimilation in reanalysis means the model is likely "as good as it gets" for a model representation in the region. ERA5 is an atmospheric reanalysis product that combines vast amounts of historical observations into global estimates using state-of-the-science modelling and data assimilation systems. It covers the earth on a 30 km horizontal resolution and resolves the atmosphere using 137 levels from the surface to a height of 80 km (Hersbach et al., 2020). ERA5 has been found to exhibit similarity with gridded datasets like CHIRPS and CenTrends (Centennial Trends; Funk et al., 2015) which incorporate most observations in Kenya Nicholson and Klotter, 2021 with considerable improvements over ERA-interim on better representation of the spatial distribution of precipitation during extreme years and reduction in climatological biases (Gleixner et al. 2020). The evaluation and rating are done independently for the two model types. We define a range of values based on the statistics of ERA5 for which the models are rated, 1 being on the lower range (worst performing), 2 middle range (medium performance), and 3 on the upper range (best performing). The scores (1, 2, and 3) are then averaged to give a mean performance (MP) of each parameter for every model. The cut-off score for AGCMs models is 2.5 while that of CGCMs models is 2.4. As the metrics span a range of scales and specificity defined based on a very generalized understanding of what constitutes a bad and a good model, we do not assign weights to individual metrics. This is the simplest approach to the problem at hand, i.e., rejecting models that do not perform well in simulating processes relevant from the point of view of the objectives of the study. As such, model selection is based on mean performance i.e., those found to deviate substantially (persistent low average performance) from ERA5, and consequently CHIRPS, are disregarded for the analysis. Detailed information on the evaluation is found in Supplementary Material S2.

2.4. Attribution analysis

We chose spatial domains for analysis in each event year that encompass the areas of Kenya with (i) above-average seasonal rainfall and (ii) documented high-impact floods. These domains were also made large enough to accommodate GCM-scale data. The domains were 3°S, 1.7°N, 34.7°E, 37°E; 3°S, 2.0°N, 34°E, 36.7°E; and 3°S, 1.7°N, 34.7°E, 39°E for 2012, 2016 & 2018, respectively (illustrated in Fig. 1). Given its importance for the impacts, we primarily focus our analysis on the change in intensity or magnitude rather than probability and thus we evaluate the magnitude ratio (MR) and the fraction of attributable magnitude (FAM) to understand the attributable change in the magnitude of heavy rainfall in the seasons when the flood events occurred. MR is the measure of how the magnitude of n-day maximum rainfall during the season has changed in the present day versus the pre-industrial period. An MR $>$ 1.0 indicates that anthropogenic climate change has increased the magnitude of the event and vice versa for MR $<$ 1.0. Following Stone and Allen (2005) definition of FAR (Fraction of Attributable Risk) for likelihood-based event attribution, we define the Fraction of Attributable Magnitude (FAM; expressed as $1 - 1/\mathrm{MR}$) as the proportion of Rx5d, Rx10d, and Rx20d that can be ascribed to anthropogenic climate change. We express FAM as percentage increase (positive values) and percentage decrease (negative values) in interpreting the changes in attributable magnitude. For instance, FAM of 100% indicates that the event or class of events of the given magnitude would never occur in the preindustrial climate and thus is entirely attributable to anthropogenic climate change, while zero indicates that there is no influence of anthropogenic climate change on the magnitude of the event. FAM greater than zero implies human influence, with the amount of human influence increasing for larger values. Negative values indicate that human influence has resulted in a decrease in the given magnitude by that given proportion. For the three experiment types (observations, atmospheric, and coupled model runs), we use different approaches to evaluate the natural and historical MRs, outlined below.

2.4.1. Attribution analysis using observations

For observations, we adopt the approach used in several recent attribution studies (e.g., Van Oldenborgh et al., 2016; Van Der Wiel et al., 2017; Philip et al., 2019). We use the generalized extreme value (GEV) distribution, an approach to extreme value analysis that allows for characterization of intensity, duration, as well as frequency of extreme events by defining extremes as block maxima (Coles, 2001). Rx5d, Rx10d, and Rx20d are seasonal maxima thus well suited for GEV analysis. Following Katz (2013), we fit a GEV to each of the three RxNds, with a 4-year smoothed global mean surface temperature (GMST) as a covariate to account for possible changes due to anthropogenic climate change over time, from which we estimate the return period and magnitude of each event in 2012, 2016 and 2018 (hereafter, event-year) with respect to preindustrial conditions (specifically, the year 1880). We then calculate MR as the ratio of event-year magnitude versus preindustrial magnitude for the same return period as that observed.

For an extreme value x, GEV function is represented by

$$F(x) = exp\left[-\left(1+\xi\frac{x-\mu}{\sigma}\right)^{1/\xi}\right]$$

$$\mu = \mu_0\, exp\left(\frac{\alpha T'}{\mu_0}\right)$$

$$\sigma = \sigma_0\, exp\left(\frac{\alpha T'}{\mu_0}\right) \quad (1)$$

Where $\boldsymbol{\mu}$ is the location parameter, $\boldsymbol{\sigma}$ is the scale parameter, and $\boldsymbol{\xi}$ represents the shape parameter of the curve. The location parameter specifies the centre of the distribution while the scale parameter determines the size of deviations around the location parameter. The shape parameter determines the tail's behaviour (negative indicates light tail while positive indicates heavy tail). $\mathbf{T}'$ is the smoothed GMST, a measure of the uniform global climate response to external forcing used to scale the GEV fit. We consider an approach where both location and scale of the distribution scale with GMST i.e., magnitude (μ) and variability (σ) of the considered weather/climate variable change as a result of global warming. The scaling is taken to be an exponential function of GMST resembling Clausius–Clapeyron (CC) scaling expected of daily precipitation extremes with local daily temperature in regions with enough moisture availability (Allen and Ingram, 2002; Trenberth et al., 2003; Trenberth, 2011; O'Gorman, 2015). To fit the distribution to the precipitation data, however, we need to make a further assumption that σ scales with μ (Hanel et al., 2009). These are minimum assumptions that have to be made as described in (Philip et al., 2020), and this is a standard approach to attribution used in numerous studies (e.g. (Van Der Wiel et al., 2017; van Oldenborgh et al., 2016). The fit parameters are estimated using the maximum likelihood estimation (MLE) method where σ, μ0 and σ0 are varied while ξ is assumed to be constant. For each event i, we, therefore, estimate the return period in the event-year then the magnitude of an event with the same return period in 1880. MR and FAM are then calculated as described earlier in Section 2.4. To sample the uncertainty of MR, we estimate 95% confidence intervals using a non-parametric bootstrap approach, by repeating the GEV fitting and magnitude estimation through 1 000 random samples, with replication, of the observed data.

2.4.2. Attribution analysis of AGCMs

For the AGCMs, we opt for a non-parametric approach because it does not require any strong assumptions about the underlying distribution, and thus is more robust. The simulations are initial-condition ensembles, so the variation between each simulation captures the stochastic nature of RxNd, while the ensemble mean represents the common (forced) signal. Therefore, in order to estimate the distribution of MR, we bootstrap RxNd for each set of attribution runs to obtain a 1 000-member resample of the mean. To do this, we select 1 000 pairs of historical and natural RxNd values with replacement from which we calculate 1 000 MRs. Basically, we take the ensemble mean of each RxNd from the historical and the natural simulations as the forced and the unforced signal, respectively. Thus, for each event i, we obtain Mi, magnitudes in the event year, and M0, magnitudes in the natural climate for every RxNd. We then calculate MR and FAM, and a median MR and FAM across the 1 000 resamples. To sample the uncertainty of MR from the distribution, we calculate the 95% sampling interval for MR and FAM from the 1 000 resamples.

2.4.3. Attribution analysis of CGCMs

For each CGCM, we use the return periods estimated in the observational analysis to evaluate changes in the event magnitudes between the current and the past climate. For this, we fit GEV to RxNd (1851–1900 and 2001–2030) without a covariate to evaluate magnitudes, for a given return period. We use present-day return periods based on CHIRPS analysis (see, Table 3) rather than KMD data, although results do not vary significantly (not shown). For every event i, therefore, we obtain Mi and M0 for each RxNd. We then calculate MR and FAM as described in Section 2.4 and adopt a bootstrapping approach to estimate the median and the 95% confidence intervals.

2.4.4. Synthesis

Since different approaches are used to evaluate MR and FAM for each experiment type, we first synthesise the results independently for each experiment type, and then combine these into an overall synthesis result. By combining the results in the synthesis step, we give a quantitative summary statement for the study. This, however, does not suggest that the best guess of that summary range is indeed any closer to the real answer to the question than the results from the individual experiments. But since none of the three experiment types provides us with

Table 3
Summary of estimated magnitude ratios and Fraction of attributable magnitude for observational data.

		2012				2016				2018			
Dataset	Metric	Return period	MR	95%CIs	FAM	Return period	MR	95%CIs	FAM	Return period	MR	95%CIs	FAM
CHIRPs	Rx5d	3.67	1.11	0.90,1.44	11%	1.45	1.20	0.85,1.65	20%	11.5	1.17	0.88,1.64	17%
	Rx10d	10.8	1.12	0.80,1.46	12%	1.58	1.22	0.76,1.82	22%	50.3	1.04	0.73,1.55	4%
	Rx20d	23.8	1.16	0.78,1.54	16%	2.38	1.21	0.73,2.01	21%	32.75	1.06	0.70,1.66	6%
KMD	Rx5d	8.1	0.97	0.74,1.31	−3%	2.87	0.97	0.68,1.43	−3%	1.82	0.98	0.74,1.43	−2%
	Rx10d	11.02	1.04	0.81,1.36	4%	2.10	1.06	0.76,1.47	6%	2.81	1.06	0.73,1.56	6%
	Rx20d	11.69	1.05	0.75,1.42	5%	2.31	1.08	0.69,1.60	8%	9.53	1.07	0.66,1.63	7%

the whole uncertainty nor are the results from different experiment types, we use the synthesis, as a numerical aid to summarise the results. This has become a common practice as described e.g Philip et al., 2020. To calculate the median for each experiment, we take the mean of the individual medians, assuming equal weighting, and then likewise for the overall synthesis result.

To estimate confidence intervals for the synthesis, we follow (Paciorek et al., 2018) in assuming that the experiment MRs (each with a median and 95% CI) distributions are not normally distributed, but that we can approximate the right and left tails as parts of two different normal distributions, with standard deviations (SD) equal to (mean – 2.5th percentile)/1.96 and (97.5th percentile – mean)/1.96, respectively. We first calculate a pooled variance (S^2) using the estimated upper and the lower SD for each attribution result:

$$S^2 = (S_1^2\,(n_1\text{-}1) + S_2^2(n_2\text{-}1))/n_1+n_2\text{-}2, \quad (2)$$

where **n** is the sample size, $\mathbf{S^2}$ is the pooled variance. For equal sample size (as in our case), equation (2) reduces to $S^2=(S_1^2+S_2^2)/2$. This can be extended for more than two samples (experiments)

$$S^2=(S_1^2+S_2^2+S_3^2+ \ldots\ldots+Sm^2)/m \quad (3)$$

where **m** is the number of experiments.

For each experiment type, we calculate lower pooled variance and upper pooled variance from which the square root gives the pooled lower (pSDl) and upper (pSD_u) standard deviation, respectively.

$$Sl^2=(S_{l1}^2+S_{l2}^2+S_{l3}^2+\ldots+Slm$$

$$Su^2=(S_{u1}^2+S_{u3}^2+ \ldots\ldots+S_{um}^2)/m$$

Where $\mathbf{Sl^2}$ and $\mathbf{Su^2}$ are the lower and upper pooled variances, respectively. The value of **m** is 2 for observations, 3 for atmospheric and

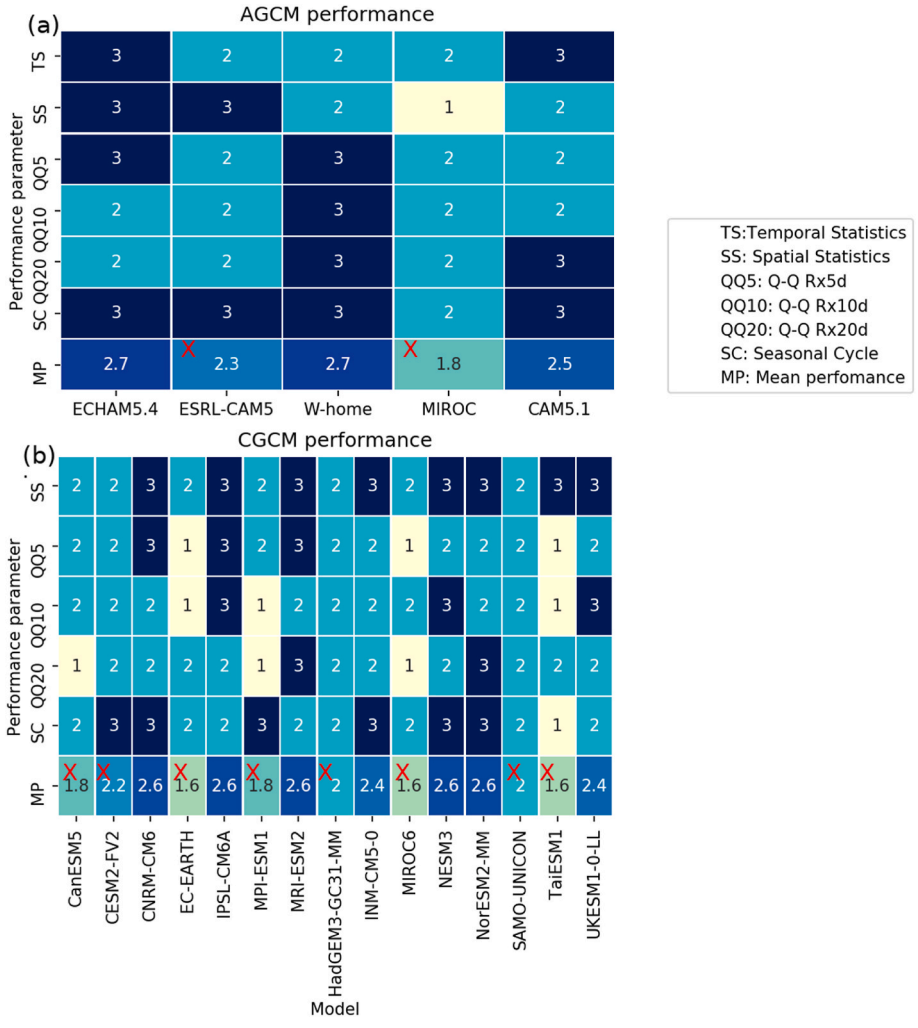

Fig. 2. Summary of model performance for **(a)** C20C+ and weather@home and **(b)** CMIP6 models based on different statistics of spatio-temporal characteristics of MAM rainfall in the study region. The numbers in the heatmap represent the average score on a scale of 1–3 (with 3 representing good and 1 bad performance), based on MAE, R, and RMSE for TS, SS, SC, QQ5, QQ10, and QQ20. MP is the mean of the average scores which gives the overall performance of each model. Models with an average score below 2.5 are marked with an X over the MP boxes and were excluded in the analysis.

7 for coupled experiments. Therefore, we take synthesis mean -(1.96pSDl) and synthesis mean +(1.96pSDu) to obtain lower and upper bound synthesis, respectively. To calculate the confidence interval for the overall synthesis, mean, we repeat the above procedure using the pooled variances from each experiment.

3. Results

3.1. Model evaluation

Fig. 2 provides a summary of AGCM and CGCM evaluation results. For convenience, we label the summary of statistics for temporal and spatial patterns as 'Temporal Statistics' (TS) and 'Spatial Statistics' (SS) respectively; 'QQ5', 'QQ10', and 'QQ20' for Rx5d, Rx10d, and Rx20d respectively from the Q-Q plots; and seasonal cycle as 'SC'. For every model, each rainfall characteristic (TS, SS, QQ5, QQ10, QQ20, and SC) is rated on a scale of 1–3 based on how close the statistics of its metrics are to that of CHIRPS and ERA5 data (see Section 2.3).

The models generally reproduce the expected bimodal rainfall regime, associated with north-south migration of the inter-tropical convergence zone (ITCZ) (see, Supplementary Material Fig. S5 and S9). However, all the models underestimate MAM rainfall intensities, while overestimating OND; this misrepresentation is generally larger in the coupled models. The same weakness has been found in CMIP5 (Tierney et al., 2015; Ongoma et al., 2018a,b; King et al., 2020), CMIP3 (Anyah and Qiu, 2012a) and weather@home2 (Uhe et al., 2018). However, Ayugi et al. (2021) found substantial performance improvement in CMIP6 over CMIP5 in representation of East African rainfall, notably, simulation of mean annual cycle and extreme indices although biases remain. AGCMs capture the distribution of RxNds, and spatial and temporal patterns of MAM rainfall season reasonably well compared to the coupled models. Overall, AGCMs are found to perform better than the coupled models. This is expected as AGCMs have their interannual variability synchronised with the observations by prescribing SST observations, unlike CGCMs. However, we do not evaluate temporal correlation for GCMs because we do not expect the variability to be synchronised.

3.2. Attribution results

3.2.1. Observational analysis

Table 3 shows changes in the magnitude ofRx5d, Rx10d, and Rx20d with their corresponding return time periods between the event-years and preindustrial period based on observational data. Attribution analysis of CHIRPS data shows an increase in the magnitude (MR $>$ 1.0) of all three extreme rainfall metrics, in each of the three event-years. For KMD data, increases in magnitude are seen for R$\times$10d and Rx20d in all three event years, but the magnitude of Rx5d decreases in all three years. The highest return periods are seen for 2018 events based on CHIRPS analysis, while KMD analysis shows the highest in 2012. The fraction of attributable magnitude ranges from -2 to 22% with highest shown by CHIRPS for 2016 across all the indices. Despite an overall increase in the intensity of extreme rainfall, the increase is statistically non-significant (lower bound on the uncertainty of MR range less than or equal to 1.0) and so we do not find an attributable human influence on heavy rainfall magnitude with this approach.

3.2.2. AGCM analysis

Table 4 shows the results of the atmospheric model analysis. Results from ECHAM5.4 and weather@home show an intensification of rainfall across all the years whereas CAM5.1 shows an increase in 2012 and 2018, but a reduction in magnitude in 2016. Overall, the largest proportion of climate change-attributable magnitude is seen in MAM 2018, although ECHAM5.4 depicts equally high values in 2012. Correspondingly, the lowest proportions of attributable magnitude are seen in 2016 across all RxNds. Statistically significant increases (95% CI of the MR does not encompass 1) in intensity are shown by weather@home in all RxNds; ECHAM5.4 for Rx20d in 2012, Rx5d and Rx10d in 2016 and Rx5d in 2018, and CAM5.1 for Rx10d and Rx20d in 2012 and RxNds in 2018. ECHAM5.4 shows higher values of fraction of attributable magnitude across the years in all indices compared to weather@home and CAM5.1. While there are still several instances where the result is not statistically significant, the result is much stronger than for the observations (lower CI close to 1.0 when it is below 1.0).

3.2.3. CGCM analysis

There is less agreement in the change of magnitude of RxNds in analyses based on CMIP6 data compared to the other two experiments (Table 5). IPSL-CM6A-LR, INM-CM5, and NorESM2-MM show a general increase while MRI-ESM2-0 shows reduction in intensity, across all the event years. UKESM1-0-LL shows a general reduction except for Rx10d and Rx20d in 2018 which depict a substantial statistically significant increase. Analysis of CNRM-CM6-1-HR shows an increase in the intensity of all RxNds in 2018 and Rx5d and Rx20d in 2012 but a reduction in 2016 and Rx20d in 2012. For NESM3, the magnitude of Rx5d increased in 2012 and 2018 while the magnitude of R$\times$10d and Rx20d for 2012 and 2018 decreased. Of these, NorESM2-MM for all RxNds in 2018 and UKESM1-0-LL for Rx5d in 2012, and Rx5d and Rx20d in 2016 show a significant positive influence of anthropogenic climate change.

3.3. Synthesis results

Fig. 3 gives a synthesis of the results, where outcomes from each experiment type are first synthesised independently after which an overall synthesis result is shown, for each of the rainfall indices, and for each event-year. Overall synthesis results show intensification of extreme rainfall in all the event years relative to a preindustrial climate across all the experiments, but without statistical significance (the 95% CI encompasses a MR of 1.0). MAM 2018 shows higher levels of intensification compared to 2012 and 2016. In 2018, intensity of Rx5d, Rx10d and Rx20d is seen to increase by 6%, 9% and 9% respectively relative to preindustrial period. For 2016, the multi-experiment mean change in magnitude is found to be 3% in Rx5d, 4% in Rx10d and Rx20d, while in 2012 the intensity of Rx5d increased by 3%, and 6% in Rx10d and

Table 4
Summary of estimated magnitude ratios and fraction of attributable magnitude from atmosphere-only attribution runs.

		2012			2016			2018		
Model	Metric	MR	95%CIs	FAM	MR	95%CIs	FAM	MR	95%CIs	FAM
weather@home2	Rx5d	1.046	1.028,1.063	4.6%	1.033	1.015,1.051	3.3%	1.073	1.052,1.096	7.3%
	Rx10	1.051	1.31,1.071	5.1%	1.036	1.018,1.055	3.6%	1.085	1.061,1.108	8.5%
	Rx20d	1.068	1.048,1.088	6.8%	1.030	1.011,1.049	3.0%	1.099	1.072,1.13	9.9%
ECHAM5.4	Rx5d	1.138	0.962,1.346	13.8%	1.109	1.009,1.226	10.9%	1.120	1.006,1.262	12%
	Rx10	1.143	0.977,1.341	14.7%	1.098	1.015,1.190	9.8%	1.111	0.994,1.239	11.1%
	Rx20d	1.186	1.000,1.387	18.6%	1.074	0.984,1.165	7.4%	1.060	0.945,1.189	6%
CAM5.1	Rx5d	1.028	0.989,1.065	2.8%	0.983	0.951,1.018	−1.7%	1.040	1.000,1.079	4%
	Rx10	1.043	1.002,1.084	4.3%	0.988	0.954,1.022	−1.2%	1.053	1.014,1.094	5.3%
	Rx20d	1.064	1.023,1.106	6.4%	0.965	0.930,1.000	−3.5%	1.045	1.009,1.081	4.5%

Table 5
Summary of estimated magnitude ratios and fraction of attributable magnitude from coupled model runs.

		2012			2016			2018		
Model	Metric	MR	95% CIs	FAM	MR	95% CIs	FAM	MR	95% CIs	FAM
CNRM-CM6-1-HR	Rx5d	1.025	0.831,1.272	2.5%	0.98	0.69,1.293	−2%	1.08	0.86,1.33	8%
	Rx10	0.979	0.785,1.152	−2.1%	0.86	0.61,1.15	−14%	1.01	0.70,1.29	1%
	Rx20d	1.028	0.856,1.181	2.8%	0.88	0.68,1.09	−12%	1.21	0.96,1.54	21%
IPSL-CM6A-LR	Rx5d	1.09	0.94,1.21	9%	1.10	0.99,1.25	10%	1.07	0.95,1.23	7%
	Rx10	1.06	0.93,1.19	6%	1.04	0.94,1.15	4%	1.01	0.84,1.13	1%
	Rx20d	1.08	0.96,1.23	8%	1.04	0.96,1.14	4%	1.02	0.88,1.15	2%
INM-CM5	Rx5d	1.27	1.09,1.58	27%	1.21	1.089,1.35	21%	1.22	0.92,1.44	22%
	Rx10	1.35	0.91,1.84	35%	1.23	0.096,1.34	23%	1.11	0.82,1.54	11%
	Rx20d	1.23	0.96,1.69	23%	1.28	1.16,1.40	28%	1.15	0.83,1.57	15%
NorESM2-MM	Rx5d	1.01	0.89,1.12	1%	0.99	0.89,1.15	1%	1.17	1.08,1.26	17%
	Rx10	1.08	0.98,1.28	8%	1.08	0.93,1.37	8%	1.34	1.13,1.57	34%
	Rx20d	1.11	0.93,1.32	11%	1.04	0.89,1.22	4%	1.44	1.16,1.75	44%
UKESM1-0-LL	Rx5d	0.68	0.51,0.90	−32%	0.78	0.50,1.36	−22%	0.83	0.33,1.19	−17%
	Rx10	0.89	0.54,1.30	−11%	0.63	0.40,1.17	−37%	1.69	1.31,3.82	69%
	Rx20d	1.10	1.01,1.78	10%	0.64	0.47,1.05	−36%	1.33	0.46,3.39	33%
NESM3	Rx5d	1.02	0.92,1.11	2%	1.05	0.92,1.18	5%	1.01	0.92,1.06	1%
	Rx10d	0.99	0.89,1.07	−1%	1.06	0.92,1.21	6%	0.96	0.88,1.11	−4%
	Rx20d	0.98	0.89,1.07	−2%	1.07	0.97,1.26	7%	0.97	0.84,1.12	−3%
MRI-ESM2-0	Rx5d	0.85	0.75,0.94	−15%	0.80	0.74,0.93	−20%	0.82	0.75,0.94	−18%
	Rx10d	0.86	0.74,0.98	−14%	0.77	0.67,0.89	−23%	0.83	0.56,1.27	−17%
	Rx20d	0.94	0.79,1.23	−6%	0.82	0.71,0.96	−18%	0.88	0.77,1.01	−12%

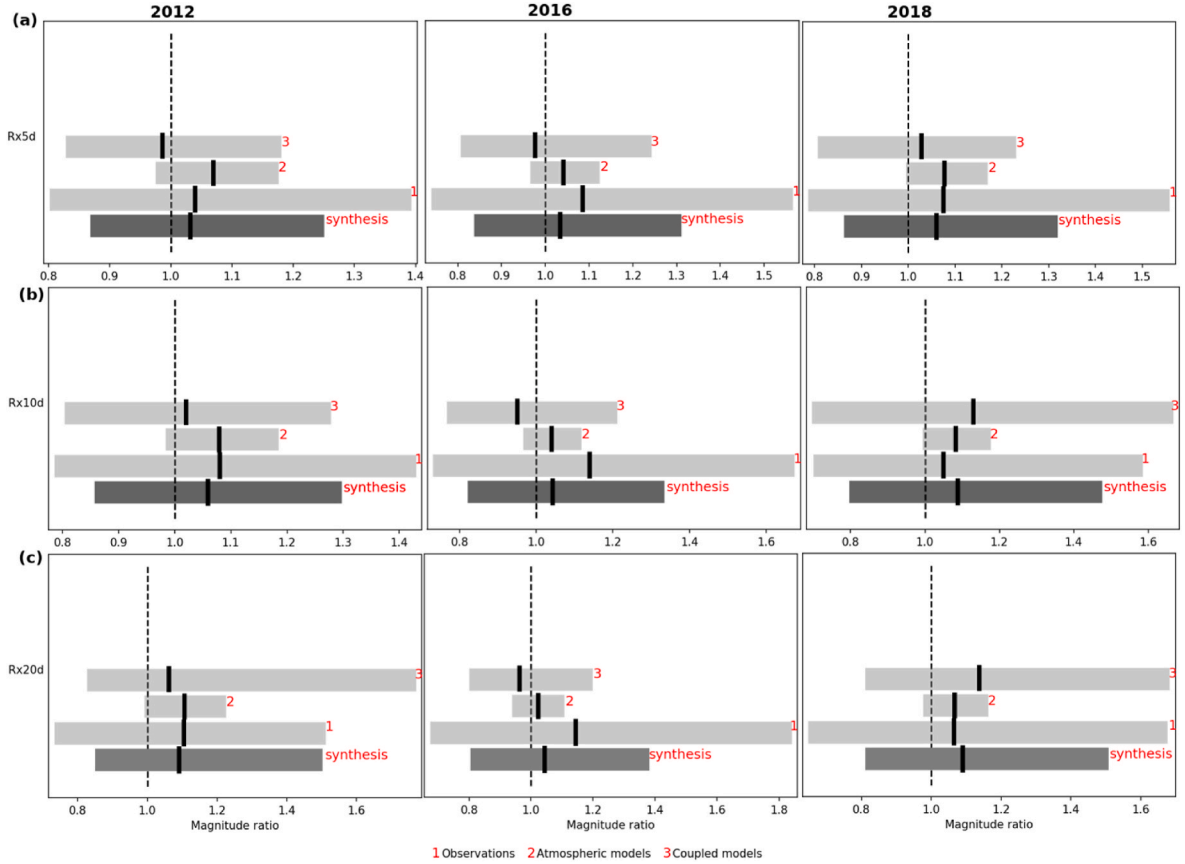

Fig. 3. Synthesis results for attribution analysis of observations, atmospheric models, and coupled models for change in magnitude of Rx5d, Rx10d and Rx20d between preindustrial period and event-year 2012, 2016, and 2018. The overall synthesis result for the three experiments is shown by the thicker bar marked 'synthesis' below the individual experiment results. The thick black marking represents the mean while the bar spans the 95% confidence interval.

Rx20d.

Results of individual experiment synthesis indicate that the intensity of MAM 2018 extreme rainfall has increased across all experiments. For Rx5d, an increase of 8% is seen in observations, 7% in atmospheric models and 3% in coupled models. For Rx10d, 5% increase is found in observations, 8% in atmospheric models and 13% in coupled models while for Rx20d, 7% increase is seen in observations and atmospheric models, and 14% in coupled models. Highest values of FAM are found in Rx20d in the synthesis of coupled models (14%). However, changes in observational data and coupled models' analysis show non-significant change in intensity. For 2016, the analysis of observations and atmospheric models shows intensification of extreme rainfall while that of

coupled models shows reduction in intensity. For Rx5d, an increase of 9% is found in observations, 4% in atmospheric models and −2% in coupled models. For Rx10d, an increase of 14% is found in observations, 4% in atmospheric models and −5% in coupled models. For Rx20d, observational analysis shows an increase of 15%, 2% in the analysis of atmospheric models and −4% in coupled models. Of these findings, none is attributable to anthropogenic climate change. In 2012, intensification of extreme rainfall is seen across all RxNds in all experiments except for Rx5d in which coupled models show a reduction of 1%. In observations and atmospheric models, x5d has increased by 4% and 7% respectively. For Rx10d, increase of 8% is seen in observations, 8% in atmospheric models and 2% in coupled models. Intensity of Rx20d has increased by 11% in observations and atmospheric models and 6% in coupled models. Changes In the intensity of Rx10d and Rx20d in the analysis of atmospheric models are attributable to anthropogenic climate change. In general, it is only atmospheric models that show a significant positive influence of anthropogenic climate change in the rainfall events.

4. Discussion and conclusions

Evaluation of the role of human-induced climate change on the magnitude of March-April-May 2012, 2016, and 2018 heavy precipitation events in defined regions in Kenya was undertaken based on three different experiments using independent event-attribution approaches. Climate model ensembles representing the preindustrial or past (period prior to the onset of large-scale industrialization and human influence on the climate) and current (MAM 2012; 2016 and 2018) climates, and two observational (station and gridded) datasets were used to evaluate changes in seasonal rainfall maxima between preindustrial and current climates, as well as their return periods. To widen the temporal definition of the events, three heavy-rainfall maxima were investigated: maximum consecutive 5-day, 10-day and 20-day (Rx5d, Rx10d and Rx20d) rainfall. This multi-method multi-model methodology allows attribution results to be independent of assumptions within specific methods and idiosyncrasies of data, and thus enhancing robustness in the assessment of human-induced changes in the extreme rainfall events. This is particularly important for attribution studies in East Africa where models generally perform poorly, in addition to limited availability of long historical observations.

Looking across all the three event years, there is a general shift towards positive FAM, although this is not statistically significant. Therefore, while there might be an emerging signal of human influence on climate causing heavier rainfall events, this is not yet formally attributable to human influence on the climate system. This is an interesting finding in the context of the 'East African climate paradox' where a contradiction exists in model projections and observed trends in MAM total rainfall —an observed overall decline in rainfall since the early 1990s while model projections show a wetting trend. It remains unclear whether a changing balance in anthropogenic forcing exists whereby past trends may have been influenced by anthropogenic aerosols while the future trends are driven by increasing concentrations of greenhouse gases (e.g., Rowell et al., 2015). Over the past decade, extreme wet conditions in the MAM season e.g., 2012 (OCHA, 2012), 2016 (KMD, 2016; IFRC, 2016), 2018 Kilavi et al. (2018); OCHA (2018), OCHA (2020) have punctuated the dominant drier conditions. However, there is still limited knowledge of past and present trends of rainfall extremes over the MAM season in Kenya as reported by various studies including Omondi et al. (2014) and Schmocker et al. (2016), mainly attributed to inadequate long and quality observations (Anyah and Qiu, 2012b; Otto et al., 2020a,b). Depending on the time periods and geographical locations evaluated, exceptions of the downward rainfall trend have been noted by various researchers. For instance, analyses done on local scales have particularly exhibited upward trends in rainfall compared to those on a regional scale (Kizza et al., 2009). Variation in results of historical trend analysis also exist (Philippon et al., 2015; Nicholson, 2016b; Thiery et al., 2016) whereby some studies show increase (e.g., Gebrechorkos et al., 2019; Ongoma et al., 2018) with some decrease e.g., Schmocker et al. (2016), depicting the high variability in space and time of precipitation extremes in Kenya. Increased variability is likely to exacerbate the historic trend of less predictable and unreliable rainfall characterised by increased frequency and intensity of droughts and floods.

It is important to note that precipitation change signals have been found to emerge more slowly in regions experiencing high climate variability especially for analysis at smaller scales where models do not capture all necessary processes to realistically simulate regional details and regionally important forcings, and with high observational uncertainties (Bindoff et al., 2013; Collins et al., 2013). Also, since rainfall in East Africa is driven by both dynamic and thermodynamic processes, it is unclear whether these processes acted in opposite direction during the events thus attenuating the anthropogenic signal, especially given the existing limitation of models in simulating intense rainfall associated with deep convection (Finney et al., 2020). There is potential to use convective permitting models in attribution analyses in East Africa, however not at this point in time. At the time of this analysis, no convection permitting simulations of sufficient length and ensemble size exist that would allow for the identification of trends in extremes. Societal adaptation to climate change in areas with high climate variability is more challenging than to an overall change since extreme weather and climate events are considered to have a higher impact than the mean climate (Parmesan et al., 2000). This poses a serious threat to Kenyan livelihoods given that the dry years in recent memory which have been perceived as harbingers of the future despite the lack of attribution, leave already vulnerable societies with uncertainties of how to prepare for a changing climate. Overall, our results show an intensification of extreme rainfall in the three years studied. A shift toward high precipitation is consistent with what is expected under an enhanced greenhouse gas climate world scenario through the Clausius-Clapeyron relationship (Boer, 1993; Allen and Ingram, 2002; Trenberth 2011; O'Gorman 2015). While there is no discernible anthropogenic climate signal on the magnitude of the recent flood-inducing rainfall events in Kenya, the projected increase in MAM rainfall and the current variability characterised by increased frequency and intensity of floods amid the general drying trend suggest the need for accurate monitoring to understand and avoid adverse impacts. This study, therefore, provides a basis for in-depth assessment of current and future trends of extreme rainfall in East Africa in adapting to changing climate risks in the already vulnerable and less resilient society. Further work is required to understand the role of anthropogenic climate change in the dynamics controlling East African MAM extreme rainfall.

Author contributions

M.N. conceived the research problem. J.K., M.N, F.O. and P.W developed the attribution framework. J.K generated the climate model data inputs and observational data. J.K. analysed the data with guidance of M.N and P.W. M.N, P.W. and F.O provided supervisory support for all aspects of the research. J.K wrote the manuscript with support from M. N. All authors contributed comments during the writing of the manuscript.

Acknowledgements

The authors acknowledge the support received from the BNP Paribas Climate Foundation and the AXA Research Fund, who supported the AXA Research Chair Pro-gramme in African Climate Risk at the University of Cape Town.

Declaration of competing interest

The authors declare that they have no known competing financial interests or personal relationships that could have appeared to influence the work reported in this paper.

Data availability

Data will be made available on request.

Appendix A. Supplementary data

Supplementary data to this article can be found online at https://doi.org/10.1016/j.wace.2022.100529.

References

Allen, M.R., Ingram, W.J., 2002. Constraints on future changes in climate and the hydrologic cycle. In: Nature (Vol. 419, Issue 6903, P. 642). Cambridge Univ. Press. https://doi.org/10.1038/nature01092.

Andrews, M.B., Ridley, J.K., Wood, R.A., Andrews, T., Blockley, E.W., Booth, B., Burke, E., Dittus, A.J., Florek, P., Gray, L.J., Haddad, S., Hardiman, S.C., Hermanson, L., Hodson, D., Hogan, E., Jones, G.S., Knight, J.R., Kuhlbrodt, T., Misios, S., et al., 2020. Historical simulations with HadGEM3-GC3.1 for CMIP6. J. Adv. Model. Earth Syst. 12 (6), e2019MS001995 https://doi.org/10.1029/2019MS001995.

Anyah, R.O., Qiu, W., 2012a. Characteristic 20th and 21st century precipitation and temperature patterns and changes over the Greater Horn of Africa. Int. J. Climatol. 32 (3), 347–363. https://doi.org/10.1002/joc.2270.

Anyah, R.O., Qiu, W., 2012b. Characteristic 20th and 21st century precipitation and temperature patterns and changes over the Greater Horn of Africa. Int. J. Climatol. 32 (3), 347–363. https://doi.org/10.1002/joc.2270.

Ayugi, B., Zhidong, J., Zhu, H., Ngoma, H., Babaousmail, H., Rizwan, K., Dike, V., 2021. Comparison of CMIP6 and CMIP5 models in simulating mean and extreme precipitation over East Africa. February. https://doi.org/10.20944/preprints202102.0111.v1.

Bindoff, N.L., Stott, P.A., AchutaRao, K.M., Allen, M.R., Gillett, N., Gutzler, D., Hansingo, K., Hegerl, G., Hu, Y., Jain, S., Mokhov, I.I., Overland, J., Perlwitz, J., Sebbari, R., Zhang, X., 2013. Detection and attribution of climate change: from global to regional. Climate change 2013: the physical science basis. Contribution of Working Group I to the Fifth Assessment Report of the Intergovernmental Panel on Climate Change 1217–1308. https://doi.org/10.1017/CBO9781107415324.028 [Stocker, T.F., D. Qin, G.-K. Plattner, M. Tignor, S.K. Allen, J. Boschung, A. Nauels, Y. Xia.

Boer, G.J., 1993. Climate change and the regulation of the surface moisture and energy budgets. Clim. Dynam. 8 (5), 225–239. https://doi.org/10.1007/BF00198617.

Boucher, O., Servonnat, J., Albright, A.L., Aumont, O., Balkanski, Y., Bastrikov, V., Bekki, S., Bonnet, R., Bony, S., Bopp, L., Braconnot, P., Brockmann, P., Cadule, P., Caubel, A., Cheruy, F., Codron, F., Cozic, A., Cugnet, D., D'Andrea, F., et al., 2020. Presentation and evaluation of the IPSL-CM6A-LR climate model. J. Adv. Model. Earth Syst. 12 (7), 1–52. https://doi.org/10.1029/2019MS002010.

Camberlin, P., Okoola, R.E., 2003. The onset and cessation of the "long rains" in eastern Africa and their interannual variability. Theor. Appl. Climatol. 75 (1–2), 43–54. https://doi.org/10.1007/s00704-002-0721-5.

Cao, J., Wang, B., Yang, Y.M., Ma, L., Li, J., Sun, B., Bao, Y., He, J., Zhou, X., Wu, L., 2018. The NUIST earth system model (NESM) version 3: description and preliminary evaluation. Geosci. Model Dev. (GMD) 11 (7), 2975–2993. https://doi.org/10.5194/gmd-11-2975-2018.

Coles, Stuart, 2001. An introduction to statistical modeling of extreme values, Springer series in statistics. Questiio 25 (2), 375.

Collins, Matthew, Krinner, G., Germany, F., Shongwe, M., Africa, S., France, S.B., Uk, B. B.B.B., Germany, V.B., Uk, O.B., France, C.B., Uk, R.C., Canada, M.E., Erich, M., Uk, R.W.L., Uk, S.L., Lucas, C., 2013. Long-term climate change: projections, commitments and irreversibility. In: Climate Change 2013 the Physical Science Basis: Working Group I Contribution to the Fifth Assessment Report of the Intergovernmental Panel on Climate Change, pp. 1029–1136. https://doi.org/10.1017/CBO9781107415324.024, 9781107057.

Danabasoglu, G., Lamarque, J.F., Bacmeister, J., Bailey, D.A., DuVivier, A.K., Edwards, J., Emmons, L.K., Fasullo, J., Garcia, R., Gettelman, A., Hannay, C., Holland, M.M., Large, W.G., Lauritzen, P.H., Lawrence, D.M., Lenaerts, J.T.M., Lindsay, K., Lipscomb, W.H., Mills, M.J., et al., 2020. The community earth system model version 2 (CESM2). J. Adv. Model. Earth Syst. 12 (2), e2019MS001916 https://doi.org/10.1029/2019MS001916.

Döscher, R., Acosta, M., Alessandri, A., Anthoni, P., Arneth, A., Arsouze, T., Bergmann, T., Bernadello, R., Bousetta, S., Caron, L.-P., Carver, G., Castrillo, M., Catalano, F., Cvijanovic, I., Davini, P., Dekker, E., Doblas-Reyes, F., Docquier, D., Echevarria, P., et al., 2021. The EC-Earth3 earth system model for the climate model Intercomparison project 6. Geosci. Model Dev. Discuss. (GMDD) 1–90. https://doi.org/10.5194/gmd-2020-446.

Eyring, V., Bony, S., Meehl, G.A., Senior, C.A., Stevens, B., Stouffer, R.J., Taylor, K.E., 2016. Overview of the coupled model Intercomparison project phase 6 (CMIP6) experimental design and organization. Geosci. Model Dev. (GMD) 9 (5), 1937–1958. https://doi.org/10.5194/gmd-9-1937-2016.

Finney, D.L., Marsham, J.H., Walker, D.P., Birch, C.E., Woodhams, B.J., Jackson, L.S., Hardy, S., 2020. The effect of westerlies on East African rainfall and the associated role of tropical cyclones and the Madden–Julian Oscillation. Q. J. R. Meteorol. Soc. 146 (727), 647–664. https://doi.org/10.1002/qj.3698.

Funk, C.C., Hoell, A., 2015. The leading mode of observed and CMIP5 ENSO-residual sea surface temperatures and associated changes in indo-pacific climate. J. Clim. 28 (11), 4309–4329. https://doi.org/10.1175/JCLI-D-14-00334.1.

Funk, C., Dettinger, M.D., Michaelsen, J.C., Verdin, J.P., Brown, M.E., Barlow, M., Hoell, A., 2008. Warming of the Indian Ocean threatens eastern and southern African food security but could be mitigated by agricultural development. Proc. Natl. Acad. Sci. U.S.A. 105 (32), 11081–11086. https://doi.org/10.1073/pnas.0708196105.

Funk, C., Husak, G., Michaelsen, J., Shukla, S., Hoell, A., Lyon, B., Hoerling, M.P., Liebmann, B., Zhang, T., Verdin, J., Galu, G., Eilerts, G., Rowland, J., 2013. Attribution of 2012 and 2003-12 rainfall deficits in eastern Kenya and southern Somalia. Bull. Am. Meteorol. Soc. 94 (9), S45–S48. https://doi.org/10.1175/BAMS-D-13-00085.1.

Funk, C, Nicholson, SE., Landsfeld, M, Klotter, D, Peterson, P, Harrison, L, et al., 2015. The Centennial Trends Greater Horn of Africa precipitation dataset. Sci. Data 2 (1).

Funk, C., Peterson, P., Landsfeld, M., Pedreros, D., Verdin, J., Shukla, S., Husak, G., Rowland, J., Harrison, L., Hoell, A., Michaelsen, J., 2015. The Climate Hazards Infrared Precipitation with Stations — a New Environmental Record for Monitoring Extremes, vols. 1–21. https://doi.org/10.1038/sdata.2015.66.

Funk, C., Harrison, L., Shukla, S., Pomposi, C., Galu, G., Korecha, D., Husak, G., Magadzire, T., Davenport, F., Hillbruner, C., Eilerts, G., Zaitchik, B., Verdin, J., 2018. Examining the role of unusually warm Indo-Pacific sea-surface temperatures in recent African droughts. Q. J. R. Meteorol. Soc. 144 (June 2017), 360–383. https://doi.org/10.1002/qj.3266.

Gebrechorkos, S.H., Hülsmann, S., Bernhofer, C., 2019. Changes in temperature and precipitation extremes in Ethiopia, Kenya, and Tanzania. Int. J. Climatol. 39 (1), 18–30. https://doi.org/10.1002/joc.5777.

Giannini, A., Lyon, B., Seager, R., Vigaud, N., 2018. Dynamical and thermodynamic Elements of modeled climate change at the East African margin of convection. Geophys. Res. Lett. 45 (2), 992–1000. https://doi.org/10.1002/2017GL075486.

Guillod, B.P., Jones, R.G., Bowery, A., Haustein, K., Massey, N.R., Mitchell, D.M., Otto, F. E.L., Sparrow, S.N., Uhe, P., Wallom, D.C.H., Wilson, S., Allen, M.R., 2017. Weather@home 2: Validation of an Improved Global-Regional Climate Modelling System. Geoscientific Model Development, pp. 1849–1872. https://doi.org/10.5194/gmd-10-1849-2017.

Gutjahr, O., Putrasahan, D., Lohmann, K., Jungclaus, J.H., Von Storch, J.S., Brüggemann, N., Haak, H., Stössel, A., 2019. Max planck institute earth system model (MPI-ESM1.2) for the high-resolution model Intercomparison project (HighResMIP). Geosci. Model Dev. (GMD) 12 (7), 3241–3281. https://doi.org/10.5194/gmd-12-3241-2019.

Hanel, M., Buishand, T.A., Ferro, C.A.T., 2009. A nonstationary index flood model for precipitation extremes in transient regional climate model simulations. J. Geophys. Res. Atmos. 114 (15), 1–16. https://doi.org/10.1029/2009JD011712.

Hannart, A., Pearl, J., Otto, F.E.L., Naveau, P., Ghil, M., 2016. Causal counterfactual theory for the attribution of weather and climate-related events. Bull. Am. Meteorol. Soc. 97 (1), 99–110. https://doi.org/10.1175/BAMS-D-14-00034.1.

Hastenrath, S., Polzin, D., Mutai, C., 2010. Circulation mechanisms of Kenya rainfall anomalies. J. Clim. 24 (2), 404–412. https://doi.org/10.1175/2010JCLI3599.1.

Haustein, K., Otto, F.E.L., Uhe, P., Schaller, N., Allen, M.R., Hermanson, L., Christidis, N., McLean, P., Cullen, H., 2016. Real-time extreme weather event attribution with forecast seasonal SSTs. Environ. Res. Lett. 11 (6) https://doi.org/10.1088/1748-9326/11/6/064006.

Hegerl, G., Zwiers, F., 2011. Use of models in detection and attribution of climate change. Wiley Interdisciplinary Reviews: Clim. Change 2 (4), 570–591. https://doi.org/10.1002/wcc.121.

Herring, S.C., Christidis, N., Hoell, A., Kossin, J.P., Schreck Iii, C.J., Stott, P.A., Quan, X. W., Hoerling, M., Smith, L., Perlwitz, J., Zhang, T., Hoell, A., Wolter, K., Eischeid, J., 2018. EXPLAINING extreme events of 2016 from A climate perspective explaining extreme events of 2016 from A climate perspective AmericAn meteorologicAl society. Bulletin of the American Meteorological Society Bulletin of the American Meteorological Society Bull. Amer. Meteor. Soc 99 (991), 54–59. https://doi.org/10.1175/BAMS-D-17-0118.1.

Hersbach, H., Bell, B., Berrisford, P., Hirahara, S., Horányi, A., Muñoz-Sabater, J., Nicolas, J., Peubey, C., Radu, R., Schepers, D., Simmons, A., Soci, C., Abdalla, S., Abellan, X., Balsamo, G., Bechtold, P., Biavati, G., Bidlot, J., Bonavita, M., et al., 2020. The ERA5 global reanalysis. Q. J. R. Meteorol. Soc. 146 (730), 1999–2049. https://doi.org/10.1002/qj.3803.

Hoell, A., Hoerling, M., Eischeid, J., Quan, X.W., Liebmann, B., 2017. Reconciling theories for human and natural attribution of recent East Africa drying. J. Clim. 30 (6), 1939–1957. https://doi.org/10.1175/JCLI-D-16-0558.1.

Hogan, E., Shelly, A., Xavier, P., 2015. The observed and modelled influence of the Madden-Julian Oscillation on East African rainfall. Meteorol. Appl. 22 (3), 459–469. https://doi.org/10.1002/met.1475.

Kenya: The 2018 Long Rains Season Assessment Report - Kenya | ReliefWeb. (n.d.).

Kew, S.F., Philip, S.Y., Hauser, M., Hobbins, M., Wanders, N., Jan Van Oldenborgh, G., Van Der Wiel, K., Veldkamp, T.I.E., Kimutai, J., Funk, C., Otto, F.E.L., 2021. Impact of precipitation and increasing temperatures on drought trends in eastern Africa. Earth System Dynamics 12 (1), 17–35. https://doi.org/10.5194/esd-12-17-2021.

Kilavi, M., MacLeod, D., Ambani, M., Robbins, J., Dankers, R., Graham, R., Helen, T., Salih, A.A.M., Todd, M.C., 2018. Extreme rainfall and flooding over Central Kenya Including Nairobi City during the long-rains season 2018: causes, predictability, and potential for early warning and actions. Atmosphere 9 (12). https://doi.org/10.3390/atmos9120472.

King, J.A., Washington, R., Engelstaedter, S., 2020. Representation of the Indian Ocean Walker circulation in climate models and links to Kenyan rainfall. Int. J. Climatol. 1–28. https://doi.org/10.1002/joc.6714. December 2019.

KMD, 2016. Republic of kenya Ministry of Environment and Natural Resources State. department of environment kenya meteorological department, pp. 1–8.
Lee, W.L., Wang, Y.C., Shiu, C.J., Tsai, I.C., Tu, C.Y., Lan, Y.Y., Chen, J.P., Pan, H.L., Hsu, H.H., 2020. Taiwan earth system model version 1: description and evaluation of mean state. Geosci. Model Dev. (GMD) 13 (9), 3887–3904. https://doi.org/10.5194/gmd-13-3887-2020.
Liebmann, B., Hoerling, M.P., Funk, C., Bladé, I., Dole, R.M., Allured, D., Quan, X., Pegion, P., Eischeid, J.K., 2014. Understanding recent eastern Horn of Africa rainfall variability and change. J. Clim. 27 (23), 8630–8645. https://doi.org/10.1175/JCLI-D-13-00714.1.
Lott, F.C., Christidis, N., Stott, P.A., 2013. Can the 2011 East African drought be attributed to human-induced climate change? Geophys. Res. Lett. 40 (6), 1177–1181. https://doi.org/10.1002/grl.50235.
Lurton, T., Balkanski, Y., Bastrikov, V., Bekki, S., Bopp, L., Braconnot, P., Brockmann, P., Cadule, P., Contoux, C., Cozic, A., Cugnet, D., Dufresne, J.L., Éthé, C., Foujols, M.A., Ghattas, J., Hauglustaine, D., Hu, R.M., Kageyama, M., Khodri, M., Boucher, O., 2020. Implementation of the CMIP6 forcing data in the IPSL-CM6A-LR model. J. Adv. Model. Earth Syst. 12 (4), 1–22. https://doi.org/10.1029/2019MS001940.
Marthews, T.R., Otto, F.E.L., Mitchell, D., Dadson, S.J., Jones, R.G., 2015. The 2014 drought in the horn of Africa: attribution of meteorological drivers. Bull. Am. Meteorol. Soc. 96 (12), S83–S88. https://doi.org/10.1175/BAMS-D-15-00115.1.
Meehl, G.A., Stocker, T.F., Collins, W.D., Friedlingstein, P., Gaye, A.T., Gregory, J.M., Kitoh, A., Knutti, R., Murphy, J.M., Noda, A., Raper, S.C.B., Watterson, I.G., Weaver, A.J., Zhao, Z.-C., 2007. Global Climate Projections. *Climate Change 2007: the Physical Science Basis. Contribution of Working Group I to the Fourth Assessment Report of the Intergovernmental Panel on Climate Change*.
NAS, 2016. Attribution of extreme weather events in the context of climate change. In: Attribution of Extreme Weather Events in the Context of Climate Change. https://doi.org/10.17226/21852.
Richard B. Neale, C.C.C., Lauritzen, A.G.P.H., Sungsu Park, DavidL., Williamson, A.J.C.R. G., Lamarque, D.K.J.-F., Mills, D.M.M., Tilmes, A.K.S.S., Vitt, Francis, Morrison, Hugh, Philip Cameron-Smith, WilliamD., Collins, Michael J., Iacono, Richard C., Easter, S.J.G., RaschXiaohongLiuPhilipJ, M.A.T., 2012. Description of the NCAR community atmosphere model (CAM 5.0). Theory of Hindi Syntax. https://doi.org/10.1515/9783111358611-006.
Nicholson, S.E., 2016a. An analysis of recent rainfall conditions in eastern Africa. Int. J. Climatol. 36 (1), 526–532. https://doi.org/10.1002/joc.4358.
Nicholson, S.E., 2016b. An analysis of recent rainfall conditions in eastern Africa. Int. J. Climatol. 36 (1), 526–532. https://doi.org/10.1002/joc.4358.
Nicholson, S.E., 2017. Climate and climatic variability of rainfall over eastern Africa. Rev. Geophys. 55 (3), 590–635. https://doi.org/10.1002/2016rg000544.
OCHA. Eastern Africa region: floods and locust outbreak Snapshot (may 2020) - Ethiopia | ReliefWeb. Retrieved May 12, 2021, from. https://reliefweb.int/report/ethiopia/eastern-africa-region-floods-and-locust-outbreak-snapshot-may-2020.
Nicholson, Sharon, Klotter, Douglas, 2021. Assessing the reliability of satellite and reanalysis estimates of rainfall in equatorial Africa. Remote Sens. 13, 3609. https://doi.org/10.3390/RS13183609.
OCHA, 2012. Eastern Africa Region: Floods and Locust Outbreak Snapshot (May 2020) - Ethiopia. ReliefWeb.
OCHA Flash Update #5: Floods in Kenya | 10 May 2018 - Kenya | ReliefWeb. (n.d.).
Omondi, P., Ogallo, L.A., Anyah, R., Muthama, J.M., Ininda, J., 2012. Linkages between global sea surface temperatures and decadal rainfall variability over Eastern Africa region. Int. J. Climatol. 33 (8), 2082–2104. https://doi.org/10.1002/joc.3578.
Omondi, P.A.o., Awange, J.L., Forootan, E., Ogallo, L.A., Barakiza, R., Girmaw, G.B., Fesseha, I., Kululetera, V., Kilembe, C., Mbati, M.M., Kilavi, M., King'uyu, S.M., Omeny, P.A., Njogu, A., Badr, E.M., Musa, T.A., Muchiri, P., Bamanya, D., Komutunga, E., 2014. Changes in temperature and precipitation extremes over the Greater Horn of Africa region from 1961 to 2010. Int. J. Climatol. 34 (4), 1262–1277. https://doi.org/10.1002/joc.3763.
Ongoma, V., Chen, H., Gao, C., 2018a. Evaluation of CMIP5 twentieth century rainfall simulation over the equatorial East Africa. Theor. Appl. Climatol. 1–18. https://doi.org/10.1007/s00704-018-2392-x. Ipcc 2013.
Ongoma, V., Chen, H., Omony, G.W., 2018b. Variability of extreme weather events over the equatorial East Africa, a case study of rainfall in Kenya and Uganda. Theor. Appl. Climatol. 131 (1– 2), 295–308. https://doi.org/10.1007/s00704-016-1973-9.
Otieno, V.O., Anyah, R.O., 2012. CMIP5 simulated climate conditions of the Greater Horn of Africa (GHA). Part II: projected climate. Clim. Dynam. 41 (7–8), 2099–2113. https://doi.org/10.1007/s00382-013-1694-z.
Otto, Friederike, 2017. Attribution of weather and climate events. Annu. Rev. Environ. Resour. https://doi.org/10.1146/annurev-environ-102016-060847.
Otto, F.E.L., Boyd, E., Jones, R.G., Cornforth, R.J., James, R., Parker, H.R., Allen, M.R., 2015. Attribution of extreme weather events in Africa: a preliminary exploration of the science and policy implications. Climatic Change 132 (4), 531–543. https://doi.org/10.1007/s10584-015-1432-0.
Otto, F.E.L., Van Oldenborgh, G.J., Eden, J., Stott, P.A., Karoly, D.J., Allen, M.R., 2016. The attribution question. Nat. Clim. Change 6 (9), 813–816. https://doi.org/10.1038/nclimate3089.
Otto, F.E.L., Harrington, L., Schmitt, K., Philip, S., Kew, S., Jan van Oldenborgh, G., Singh, R., Kimutai, J., Wolski, P., 2020a. Challenges to understanding extreme weather changes in lower income countries. Bull. Am. Meteorol. Soc. 1–19. https://doi.org/10.1175/bams-d-19-0317.1. *pre*print(2020.
Otto, F.E.L., Harrington, L., Schmitt, K., Philip, S., Kew, S., van Oldenborgh, G.J., Singh, R., Kimutai, J., Wolski, P., 2020b. Challenges to understanding extreme weather changes in lower income countries. Bull. Am. Meteorol. Soc. 101 (10), E1851–E1860. https://doi.org/10.1175/BAMS-D-19-0317.1.
O'Gorman, P.A., 2015. Precipitation extremes under climate change. Curr. Clim. Change Rep. 1 (2), 49–59. https://doi.org/10.1007/s40641-015-0009-3.
Paciorek, C.J., Stone, D.A., Wehner, M.F., 2018. Quantifying statistical uncertainty in the attribution of human influence on severe weather. Weather Clim. Extrem. 20 (December 2017), 69–80. https://doi.org/10.1016/j.wace.2018.01.002.
Park, Sungsu, Shin, J. (n.d.. NCC NorESM2-MM model output prepared for CMIP6 CMIP historical. Retrieved June 4, 2021, from. https://cera-www.dkrz.de/WDCC/ui/cerasearch/cmip6?input=CMIP6.CMIP.SNU.SAM0-UNICON.piControl.
Parmesan, C., Root, T.L., Willig, M.R., 2000. Impacts of extreme weather and climate on terrestrial biota. Bull. Am. Meteorol. Soc. 81 (3), 443–450. https://doi.org/10.1175/1520-0477(2000)081<0443:IOEWAC>2.3.CO;2.
Philip, S., Sparrow, S., Kew, S.F., Van Der Wiel, K., Wanders, N., Singh, R., Hassan, A., Mohammed, K., Javid, H., Haustein, K., Otto, F.E.L., Hirpa, F., Rimi, R.H., Saiful Islam, A.K.M., Wallom, D.C.H., Jan Van Oldenborgh, G., 2019. Attributing the 2017 Bangladesh floods from meteorological and hydrological perspectives. Hydrol. Earth Syst. Sci. 23 (3), 1409–1429. https://doi.org/10.5194/hess-23-1409-2019.
Philip, S., Kew, S., van Oldenborgh, G.J., Otto, F., Vautard, R., van der Wiel, K., King, A., Lott, F., Arrighi, J., Singh, R., van Aalst, M., 2020. A protocol for probabilistic extreme event attribution analyses. Adv. Statistical Climatol. Meteorol. Oceanography 6 (2), 177–203. https://doi.org/10.5194/ascmo-6-177-2020.
Philippon, N., Camberlin, P., Moron, V., Boyard-Micheau, J., 2015. Anomalously wet and dry rainy seasons in Equatorial East Africa and associated differences in intra-seasonal characteristics. Clim. Dynam. 45 (7–8), 1819–1840. https://doi.org/10.1007/s00382-014-2436-6.
Pohl, B., Camberlin, P., 2006. Influence of the Madden-Julian Oscillation on East African rainfall. II. March-May season extremes and interannual variability. Q. J. R. Meteorol. Soc. 132 (621), 2541–2558. https://doi.org/10.1256/qj.05.223.
Pohl, B., Camberlin, P., 2011. Intraseasonal and interannual zonal circulations over the Equatorial Indian Ocean. Theor. Appl. Climatol. 104 (1–2), 175–191. https://doi.org/10.1007/s00704-010-0336-1.
Roeckner, E., Bäuml, G., Bonaventura, L., Brokopf, R., Giorgetta, M.Esch M., Hagemann, S., KirchnerL, I., Manzini, E., Rhodin, A., Schlese, U., Schulzweida, U., Tompkins Hamburg, A., 2003. The atmospheric general circulation model ECHAM5. J. Geophys. Res. Atmos. 115 (18) https://doi.org/10.1029/2010JD014036.
Roeckner, E., Brokopf, R., Esch, M., Giorgetta, M., Hagemann, S., Kornblueh, L., Manzini, E., Schlese, U., Schulzweida, U., 2006. Sensitivity of simulated climate to horizontal and vertical resolution in the ECHAM5 atmosphere model. J. Clim. 19 (16), 3771–3791. https://doi.org/10.1175/JCLI3824.1.
Rowell, D.P., Booth, B.B.B., Nicholson, S.E., Good, P., 2015. Reconciling past and future rainfall trends over East Africa. J. Clim. 28 (24), 9768–9788. https://doi.org/10.1175/JCLI-D-15-0140.1.
Rowell, D.P., Senior, C.A., Vellinga, M., Graham, R.J., 2016. Can climate projection uncertainty be constrained over Africa using metrics of contemporary performance? Climatic Change 134 (4), 621–633. https://doi.org/10.1007/s10584-015-1554-4.
Schmocker, J., Liniger, H.P., Ngeru, J.N., Brugnara, Y., Auchmann, R., Brönnimann, S., 2016. Trends in mean and extreme precipitation in the Mount Kenya region from observations and reanalyses. Int. J. Climatol. 36 (3), 1500–1514. https://doi.org/10.1002/joc.4438.
Seland, Ø., Bentsen, M., Seland Graff, L., Olivié, D., Toniazzo, T., Gjermundsen, A., Debernard, J.B., Gupta, A.K., He, Y., Kirkevåg, A., Schwinger, J., Tjiputra, J., Schancke Aas, K., Bethke, I., Fan, Y., Griesfeller, J., Grini, A., Guo, C., Ilicak, M., et al., 2020. The Norwegian earth system model, NorESM2 – evaluation of theCMIP6 DECK and historical simulations. Geosci. Model Dev. Discuss. (GMDD) 1–68. https://doi.org/10.5194/gmd-2019-378. *February*.
Sellar, A.A., Jones, C.G., Mulcahy, J.P., Tang, Y., Yool, A., Wiltshire, A., O'Connor, F.M., Stringer, M., Hill, R., Palmieri, J., Woodward, S., de Mora, L., Kuhlbrodt, T., Rumbold, S.T., Kelley, D.I., Ellis, R., Johnson, C.E., Walton, J., Abraham, N.L., et al., 2019. UKESM1: description and evaluation of the U.K. Earth system model. J. Adv. Model. Earth Syst. 11 (12), 4513–4558. https://doi.org/10.1029/2019MS001739.
Sillmann, J., Kharin, V.V., Zhang, X., Zwiers, F.W., Bronaugh, D., 2013. Climate extremes indices in the CMIP5 multimodel ensemble: Part 1. Model evaluation in the present climate. J. Geophys. Res. Atmos. 118 (4), 1716–1733. https://doi.org/10.1002/jgrd.50203.
Stone, D.A., Allen, M.R., 2005. The end-to-end attribution problem: from emissions to impacts. Climatic Change 71 (3), 303–318. https://doi.org/10.1007/s10584-005-6778-2.
Stone, D.A., Risser, M.D., Angélil, O.M., Wehner, M.F., Cholia, S., Keen, N., Krishnan, H., O'Brien, T.A., Collins, W.D., 2018. A basis set for exploration of sensitivity to prescribed ocean conditions for estimating human contributions to extreme weather in CAM5.1-1degree. Weather Clim. Extrem. 19 (August 2017), 10–19. https://doi.org/10.1016/j.wace.2017.12.003.
Stone, D.A., Christidis, N., Folland, C., Perkins-kirkpatrick, S., 2019. Authors Experiment Design of the International CLIVAR C20C + Detection and Attribution Project. https://doi.org/10.1016/j.wace.2019.100206.
Stott, P.A., Christidis, N., Otto, F.E.L., Sun, Y., Vanderlinden, J.P., van Oldenborgh, G.J., Vautard, R., von Storch, H., Walton, P., Yiou, P., Zwiers, F.W., 2016. Attribution of extreme weather and climate-related events. Wiley Interdisciplinary Reviews: Clim. Change 7 (1), 23–41. https://doi.org/10.1002/wcc.380.
Sun, Q., Miao, C., 2018. 20. Extreme rainfall (R20MM, RX5day) in Yangtze–Huai, China, in June–July 2016: the role of ENSO and anthropogenic climate change. Bull. Am. Meteorol. Soc. 99 (1), S102–S106. https://doi.org/10.1175/BAMS-D-17-0091.1.
Swart, N.C., Cole, J.N.S., Kharin, V.V., Lazare, M., Scinocca, J.F., Gillett, N.P., Anstey, J., Arora, V., Christian, J.R., Hanna, S., Jiao, Y., Lee, W.G., Majaess, F., Saenko, O.A., Seiler, C., Seinen, C., Shao, A., Sigmond, M., Solheim, L., et al., 2019. The Canadian earth system model version 5 (CanESM5.0.3). Geosci. Model Dev. (GMD) 12 (11), 4823–4873. https://doi.org/10.5194/gmd-12-4823-2019.

Tatebe, H., Ogura, T., Nitta, T., Komuro, Y., Ogochi, K., Takemura, T., Sudo, K., Sekiguchi, M., Abe, M., Saito, F., Chikira, M., Watanabe, S., Mori, M., Hirota, N., Kawatani, Y., Mochizuki, T., Yoshimura, K., Takata, K., O'Ishi, R., et al., 2019. Description and basic evaluation of simulated mean state, internal variability, and climate sensitivity in MIROC6. Geosci. Model Dev. (GMD) 12 (7), 2727–2765. https://doi.org/10.5194/gmd-12-2727-2019.

Thiery, W., Davin, E.L., Seneviratne, S.I., Bedka, K., Lhermitte, S., Van Lipzig, N.P.M., 2016. Hazardous thunderstorm intensification over lake victoria. Nat. Commun. 7, 1–7. https://doi.org/10.1038/ncomms12786.

Thiessen, A.H., 1911. Precipitation averages for large areas. Mon. Weather Rev. 39 (7), 1082–1089. https://doi.org/10.1175/1520-0493(1911)39<1082b:pafla>2.0.co;2.

Tierney, J.E., Ummenhofer, C.C., DeMenocal, P.B., 2015. Past and future rainfall in the horn of Africa. Sci. Adv. 1 (9), 1–8. https://doi.org/10.1126/sciadv.1500682.

Trenberth, K.E., 2011. Changes in precipitation with climate change. Clim. Res. 47 (1–2), 123–138. https://doi.org/10.3354/cr00953.

Trenberth, K.E., Dai, A., Rasmussen, R.M., Parsons, D.B., 2003. The changing character of precipitation. Bull. Am. Meteorol. Soc. 84 (9), 1205–1217+1161. https://doi.org/10.1175/BAMS-84-9-1205.

Uhe, P., Philip, S., Kew, S., Shah, K., Kimutai, J., Mwangi, E., van Oldenborgh, G.J., Singh, R., Arrighi, J., Jjemba, E., Cullen, H., Otto, F., 2018. Attributing drivers of the 2016 Kenyan drought. Int. J. Climatol. 38, e554–e568. https://doi.org/10.1002/joc.5389.

Van Der Wiel, K., Kapnick, S.B., Jan Van Oldenborgh, G., Whan, K., Philip, S., Vecchi, G. A., Singh, R.K., Arrighi, J., Cullen, H., 2017. Rapid attribution of the August 2016 flood-inducing extreme precipitation in south Louisiana to climate change. Hydrol. Earth Syst. Sci. 21 (2), 897–921. https://doi.org/10.5194/hess-21-897-2017.

Van Oldenborgh, G.J., Otto, F.E.L., Haustein, K., Achutarao, K., 2016. 17. The heavy precipitation event of December 2015 in Chennai, India. Bull. Am. Meteorol. Soc. 97 (12), S87–S91. https://doi.org/10.1175/BAMS-D-16-0129.1.

van Oldenborgh, G.J., Philip, S., Aalbers, E., Vautard, R., Otto, F., Haustein, K., Habets, F., Singh, R., Cullen, H., 2016. Rapid attribution of the May/June 2016 flood-inducing precipitation in France and Germany to climate change. Hydrol. Earth Syst. Sci. Discuss. 1–23. https://doi.org/10.5194/hess-2016-308. *June*.

Vellinga, M., Milton, S.F., 2018. Drivers of Interannual Variability of the East African "Long Rains.

Vigaud, N., Lyon, B., Giannini, A., 2016. Sub-seasonal teleconnections between convection over the Indian Ocean, the East African long rains and tropical Pacific surface temperatures. Int. J. Climatol. 37 (3), 1167–1180. https://doi.org/10.1002/joc.4765.

Voldoire, A., Saint-Martin, D., Sénési, S., Decharme, B., Alias, A., Chevallier, M., Colin, J., Guérémy, J.F., Michou, M., Moine, M.P., Nabat, P., Roehrig, R., Salas y Mélia, D., Séférian, R., Valcke, S., Beau, I., Belamari, S., Berthet, S., Cassou, C., et al., 2019. Evaluation of CMIP6 DECK experiments with CNRM-CM6-1. J. Adv. Model. Earth Syst. 11 (7), 2177–2213. https://doi.org/10.1029/2019MS001683.

Volodin, E., Gritsun, A., 2018. Simulation of observed climate changes in 1850-2014 with climate model INM-CM5. Earth System Dynamics 9 (4), 1235–1242. https://doi.org/10.5194/esd-9-1235-2018.

Volodin, E.M., Mortikov, E.V., Kostrykin, S.V., Galin, V.Y., Lykossov, V.N., Gritsun, A.S., Diansky, N.A., Gusev, A.V., Iakovlev, N.G., 2017. Simulation of the present-day climate with the climate model INMCM5. Clim. Dynam. 49 (11–12), 3715–3734. https://doi.org/10.1007/s00382-017-3539-7.

Yukimoto, S., Kawai, H., Koshiro, T., Oshima, N., Yoshida, K., Urakawa, S., Tsujino, H., Deushi, M., Tanaka, T., Hosaka, M., Yabu, S., Yoshimura, H., Shindo, E., Mizuta, R., Obata, A., Adachi, Y., Ishii, M., 2019. The meteorological research institute Earth system model version 2.0, MRI-ESM2.0: description and basic evaluation of the physical component. J. Meteorol. Soc. Jpn. 97 (5), 931–965. https://doi.org/10.2151/jmsj.2019-051.

Zhang, X., Alexander, L., Hegerl, G.C., Jones, P., Tank, A.K., Peterson, T.C., Trewin, B., Zwiers, F.W., 2011. Indices for monitoring changes in extremes based on daily temperature and precipitation data. Wiley Interdisciplinary Reviews: Clim. Change 2 (6), 851–870. https://doi.org/10.1002/wcc.147.